ACS OMEGA

Open Access

http://pubs.acs.org/journal/acsodf

Article

Blackberry Seeds-Derived Carbon as Stable Anodes for Lithium-Ion Batteries

Chandra Sekhar Bongu, Abeer Shiraz Khan, Muhammad Arsalan, and Edreese H. Alsharaeh*

Cite This: *ACS Omega* 2024, 9, 16725−16733

Read Online

ACCESS | Metrics & More | Article Recommendations | Supporting Information

ABSTRACT: The suitability of biocarbons derived from blackberry seeds as anode materials in lithium-ion batteries has been assessed for the first time. Blackberry seeds have antibacterial, anticancer, antidysentery, antidiabetic, antidiarrheal, and potent antioxidant properties and are generally used for herbal medical purposes. Carbon is extracted from blackberries using a straightforward carbonization technique and activated with KOH at temperatures 700, 800, and 900 °C. The physical characterization demonstrates that activated blackberry seeds-derived carbon at 900 °C (ABBSC-900 °C) have well-ordered graphene sheets with high defects compared to the ABBSC-700 °C and ABBSC-800 °C. It is discovered that an ABBSC-900 °C is mesoporous, with a notable Brunauer−Emmett−Teller surface area of 65 m^2 g^{-1}. ABBSC-900 has good electrochemical characteristics, as studied under 100 and 1000 mA g^{-1} discharge conditions when used as a lithium intercalating anode. Delivered against a 500 mA g^{-1} current density, a steady reversible capacity of 482 mA h g^{-1} has been achieved even after 200 cycles. It is thought that disordered mesoporous carbon with a large surface area account for the improved electrochemical characteristics of the ABBSC-900 anode compared to the other ABBSC-700 and ABBSC-800 carbons. The research shows how to use a waste product, ABBSC, as the most desired anode for energy storage applications.

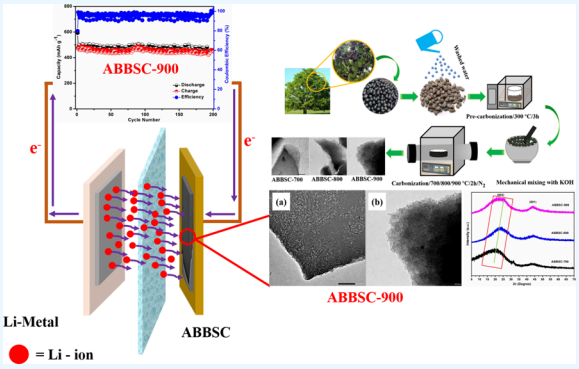

1. INTRODUCTION

The economy is growing quickly and so is the need for energy, particularly for renewable energy sources and hybrid electric vehicles. The energy storage area benefits from rechargeable lithium-ion batteries (LIBs) due to their extended cycle life, high specific energy, high working voltage, and friendly environment.[1−5] As is well-known, graphite is the primary source of conventional anode material for LIBs because of the inexpensive and electrochemical potential of lithium metal. Regrettably, graphite has a weak specific capacity, a greater irreversible capacity, polarization under high-rate discharge conditions, and poorer Coulombic efficiency behavior. Its theoretical specific capacity is 372 mA h g^{-1}.[6,7] Much work has been done to create new carbonaceous materials for helpful use.

The next generation of high-capacity anode materials (1000−4000 mA h g^{-1}), including metals (Si,[8−10] Sn[11−13]) and metal oxides (transition metal oxides (CuO, MnO_2, Mn_2O_3, Fe_2O_3, and Co_3O_4), have garnered a lot of attention recently.[14−22] Unfortunately, even at low current densities, their practical performance falls far short of expectations due to quick capacity fading.[23,24] According to studies, this issue is mainly brought about by the significant volume changes that these electrode materials undergo during the cycling processes. As a result, the electrode will continue to disintegrate and pulverize, creating a loss of electrical connections between surrounding particles.[25] Therefore, researchers focus more on the most sustainable electrode material for creating the next generation of high-performance LIBs from carbonaceous material from inexpensive renewable resources by utilizing low-energy procedures.

Recently, carbonaceous anode materials from biomass sources have gained popularity due to their abundance, affordability, ease of accessibility, and environmental friendliness.[26] However, biomass-derived carbons have suitable properties to store lithium ions with high surface area, high porousness, and good electrical conductivity.[27−29] The biomass-derived carbonaceous from cherry pits,[30] spongy pomelo peels,[31] rice husk,[32] rice straw,[33] sugar cane bagasse,[34] coffee beans,[35] coconut shells,[36] loofah,[37] honey,[38] walnut shells,[39] and bamboo and wood[40] have gained much attention in LIBs due to their extreme electrochemical properties. Because of this, the study of energy storage has given much attention to biomass use.

Received: January 24, 2024
Revised: March 13, 2024
Accepted: March 19, 2024
Published: March 29, 2024

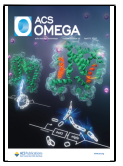

Scheme 1. Schematic Illustration of the Activated Blackberry Seeds-Derived Carbon Material Preparation

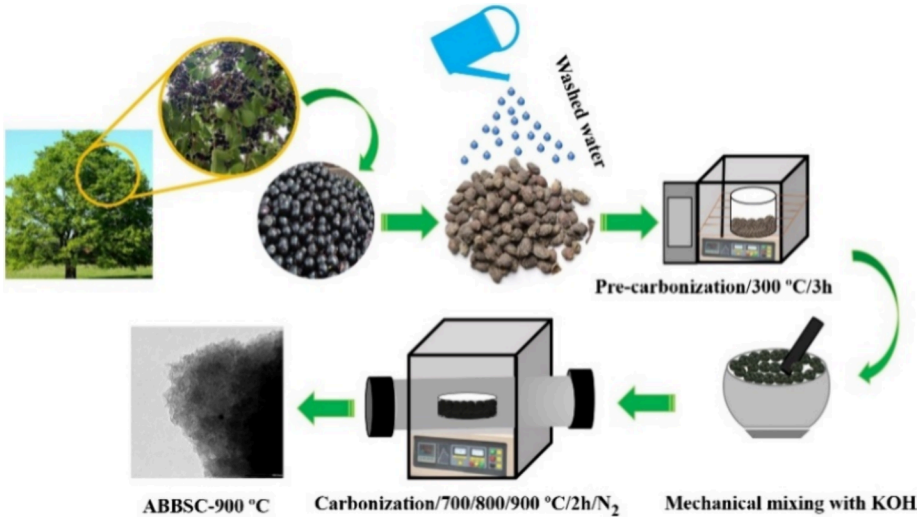

The blackberry, often referred to as jamun, is a tiny fruit that is underappreciated but has significant nutritional and medicinal value.[41] Fruit is an excellent source of antioxidants, pectin, vitamins, minerals, and anthocyanins.[42] Originating in Indonesia and India, it is widely distributed throughout Southern Asia and thrives in tropical and subtropical climates. However, blackberry seeds are used in traditional medicine to treat different ailments, including cough, dysentery, and inflammation.[43] Most importantly, blackberry seeds are used to treat diabetes mellitus.[44] The blackberry seeds with a single plant produce 170,000−400,000 seeds per year. Blackberry seeds are usually removed during processing by the food industry. Blackberry seed flour is a byproduct of the oil production process, and blackberry seeds are used to make the seed oil. In this work, we synthesized activated blackberry seeds-derived carbon (ABBSC) pyrolyzed at different temperatures (700, 800, and 900 °C) with a low-cost and environmentally friendly approach from raw blackberry seeds and used it as an anode material for LIB. ABBSC derived at 900 °C delivered 320 mA h g^{-1} at a current density of 1000 mA g^{-1}, when used as anode material for LIBs. Additionally, after 200 cycles, the ABBSC-900 material maintains a high capacity of 466 mA h g^{-1} at a high current density of 500 mA g^{-1}, demonstrating its great stability for LIBs. One of the most promising carbons to serve as anode materials for lithium-ion storage may be the ABBSC.

2. EXPERIMENTAL SECTION

2.1. Materials. Without additional purification, all of the chemicals used in the manuscript were purchased from Sigma-Aldrich and LabChem. Blackberry seeds are collected from the local fruit vendors market, washed with triple distilled water, and used for preparing the carbon material.

2.2. Synthesis of ABBSC. The biocarbon obtained from the blackberry seeds was produced as described below. The blackberry seeds were collected from a local market, washed with triple distilled water, and dried at 150 °C under the oven. Under nitrogen flow at 300 °C for 3 h, precarbonization was carried out. The precarbonized seeds were crushed and mixed with KOH (1:2) and heated at different temperatures, 700, 800, and 900 °C for 3 h in a nitrogen atmosphere with a heating rate of 5 °C min^{-1}. The final ABBSC product, a dry powder, was obtained by repeatedly washing the resulting black powder in 1 M HCl solution with triple distilled water to eliminate impurities and achieve a neutral pH. The black powder was then vacuum-dried at 80 °C. The synthesized carbon powders were denoted as ABBSC-700, ABBSC-800, and ABBSC-900 and studied further characterizations.

2.3. Physical and Electrochemical Characterizations. X-ray diffraction of the sample was recorded using a Bruker D8 Advance X-ray diffractometer (Cu−K radiation (λ = 1.5406 Å)). Utilizing WITec Raman spectroscopy, green laser light (λ = 532 nm) with an excitation energy of 2.33 eV was employed to get Raman spectra. By using JEOL-JEM-2011(200 kV) and JEOL-JSM-700F instruments, we studied the field emission scanning electron microscopy (SEM) and transmission electron microscopy (TEM) images, respectively. Using the Barrett−Joyner−Halenda (BJH) and Brunauer−Emmett−Teller (BET) procedures, the ABBSC material pore diameter and specific surface area were determined by using Autosorb iQ, Quantachrome, USA. Cyclic voltammetry (CV) was performed at a scan rate of 0.05 mV s^{-1} and within the potential window of 0.01−3.0 V by using a Biologic Science Instrument VMP3 multichannel potentiostat−galvanostat system. However, electrochemical impedance spectroscopy (EIS) measurements were carried out at room temperature at an amplitude voltage of 10 mV and a frequency range of 10 kHz to 100 mHz utilizing a Biologic VSP electrochemical workstation.

2.4. Electrode Fabrication and Assembly of the Coin Cell. To create the working electrode slurry, the active material, carbon black, and poly(vinylidene fluoride) were mixed in an 80:10:10 weight ratio in *N*-methyl pyrrolidone solution. The slurry was applied to the Cu foil with a thickness of 100 μm with the doctor blade method, and it was vacuum-dried for 12 h at 80 °C for LIB. After drying, the coated electrode was hot roll to provide better adhesion and punched the electrodes of 15 mm diameter. The active material mass loading of the electrodes was 1−2 mg. The coin cell assembly were carried out in a glovebox (MTI) with oxygen and water contents below 0.1 ppm. The half-cells (2032-coin cells) were prepared using a separator as polypropylene, 1 M $LiPF_6$ dissolved in ethylene carbonate/dimethyl carbonate (1:1 by

https://doi.org/10.1021/acsomega.4c00797
ACS Omega 2024, 9, 16725−16733

volume) as electrolyte and lithium as counter and reference electrode as received.

3. RESULTS AND DISCUSSION

3.1. Physical Characterization. Scheme 1 depicts the synthetic method of creating carbon generated from activated blackberry seeds, further elaborated in Section 2.2 on material synthesis. Two distinct broadened peaks are visible in the X-ray diffraction pattern (Figure 1) at 2θ = 20° and 43°, both of

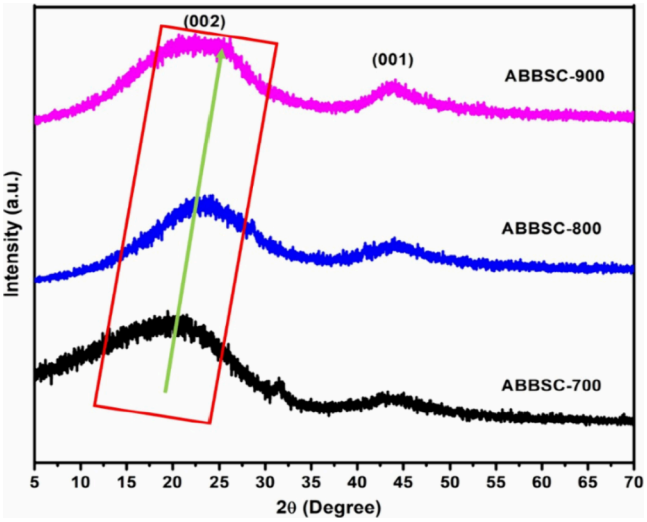

Figure 1. X-ray diffraction profiles of ABBSC-700, ABBSC-800, and ABBSC-900.

which have low intensity. These peaks can be attributed to the graphitic planes (002) and (100), which correspond to the ABBSC that is currently being synthesized at different temperatures, 700, 800, and 900 °C, respectively. The broad peaks point to these carbon compounds' amorphous nature, perhaps including a few layers with a modest degree of crystallinity that resemble graphene, which is beneficial to lithium-ion intercalation and deintercalation. The position of the (002) peak shifts to the higher 2θ direction as the heating temperature increases from 700 to 900 °C. This indicates that the structural transformation of disorder into short-range order and ultimately into a state of thermodynamic stability is responsible for decreased interplanar space between (002) planes. Based on Bragg's law, the interlayer spacings of the ABBSC-700, ABBSC-800, and ABBSC-900 were 4.14, 3.8, and 3.6 Å. The ABBSC-900 sample has the shortest interlayer spacing among the three samples. However, it is still significantly more significant than the graphite sample, which has a d_{002} value of 3.35 Å.[45] Once more, this indicates that increased temperature enhances the graphitization process and reduces the interlayer spacing during the pyrolysis process. Notably, partial carbon graphite formation can effectively raise the reversible capacity of lithium-ion intercalation.[46] Additionally, the *R*-value, which is thought to be a sign of the ordered/disordered nature of ABBSC, has been determined to comprehend the graphene sheet's structure better and, in particular, to ascertain the number of layers that make up its structure.[47] ABBSC-700, ABBSC-800, and ABBSC-900 materials have *R* values of 2.72, 2.8, and 2.92, corresponding to the (002) crystallographic plane (calculated from eq 1). ABBSC-900 *R*-value supports the presence of numerous parallel-stacked graphene sheets. The findings show that larger graphite crystallites and more ordered stacked graphite layers were produced at high pyrolysis temperatures. Improved electric conductivity is another benefit of high-temperature carbon pyrolysis (ABBSC-900), which is suitable for electrochemical performance.

$$R = \frac{B}{A} \tag{1}$$

The carbons' structural ordering and chemical structure were examined using Raman spectroscopy. Figure 2 shows the

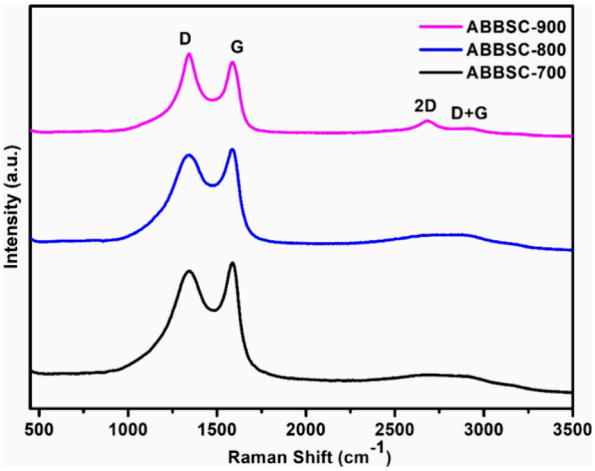

Figure 2. Raman spectra of the ABBSC-700, ABBSC-800, and ABBSC-900 carbons.

Raman results, obtained in the 400−3500 cm^{-1} region. Two peaks, centered at 1330 cm^{-1} (D band) and 1590 cm^{-1} (G band), are present in three samples. The G band corresponds to the E_{2g} vibration mode of sp^2-hybridized carbon rings, and the disorder-induced D band represents the A_{1g} breathing mode of the sp^2-hybridized carbon rings.[48] The degree of disorder in the carbons is indicated by the intensity ratio (I_D/I_G) of the G band to the D band. The intensity ratio (I_D/I_G) of the ABBSC-700, ABBSC-800, and ABBSC-900 carbon materials is 0.98, 0.99, and 1.0, respectively. The intensity ratio of the D band to the G band, representing the degree of graphitization, progressively increased with increasing heat-treatment temperature, suggesting improved electrical conductivity (promoting the Li storage and enhancing the reversible capability).[49] The second order of the D band (2D band) and D + G band corresponds to the peaks seen at 2683 and 2933 cm^{-1}. It is interesting to note that, aside from single-layer graphene, the low-intensity 2D band suggests that there may be a few additional graphene layers in the ABBSC being investigated. Furthermore, the discovery of the D + G band might be the result of nano- and polycrystalline graphitic carbon bonded to amorphous carbon.

Further, to study the morphology of the carbon generated from blackberry seeds activated with KOH at different temperatures, SEM (Figure 3) and TEM (Figure 4) measurements were conducted on the samples of ABBSC-700, ABBSC-800, and ABBSC-900. Figure 3 shows the SEM images of ABBSC-700 (Figure 3a−c), ABBSC-800 (Figure 3d−f), and ABBSC-900 (Figure 3g−i). The SEM showed an irregular sheet-like structure with smooth surfaces. SEM images revealed

https://doi.org/10.1021/acsomega.4c00797
ACS Omega 2024, 9, 16725−16733

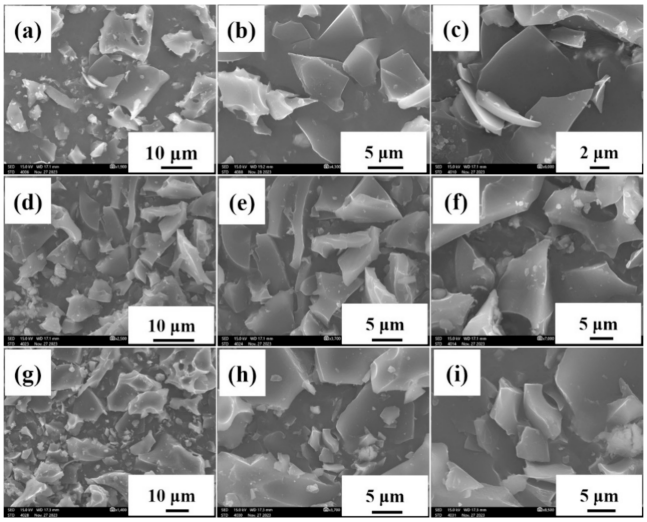

Figure 3. SEM images of (a–c) ABBSC-700, (d–f) ABBSC-800, and (g–i) ABBSC-900.

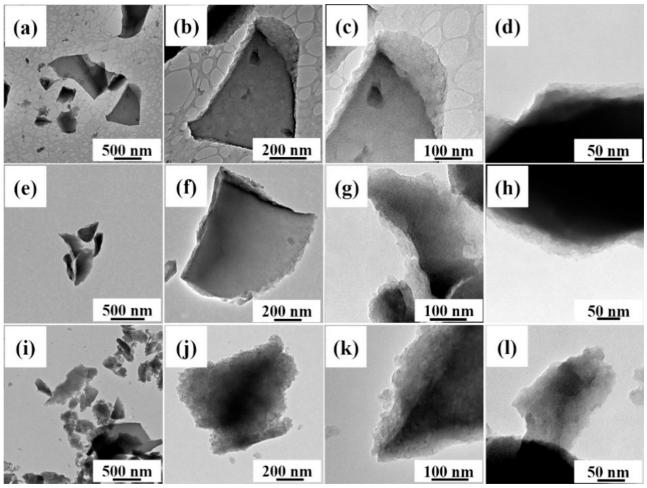

Figure 4. TEM images of (a–d) ABBSC-700, (e–h) ABBSC-800, and (i–l) ABBSC-900.

the carbon generated at 900 °C displayed smaller particles than carbon derived at 700 and 800 °C. This is because the carbon that has been pyrolyzed at a higher temperature has more graphitic domains, which can be crushed more readily during grinding.[31] The Raman and XRD data corroborate this outcome, as well. The structure of the treated ABBSCs was further confirmed with the TEM technique and represented in Figure 4. From the TEM images, ABBSC-700 (Figure 4a–d), ABBSC-800 (Figure 4e–h), and ABBSC-900 (Figure 4i–l) show transparent sheet-like structures. The size of the ABBSC-900 sheets was smaller than ABBSC-700 and ABBSC-800, which well agree with the SEM images. However, the pyrolysis temperature was increased and the formation of the pores was observed on the carbon ABBSC-900 sheets (Figure S1).

BET surface area analysis is an essential method for the evaluation of carbons because the pore size distribution, specific surface area, and total pore volume of the active material have significant influences on the electrochemical performance. Figure S2 displays the N_2 adsorption/desorption tests to understand the isotherms and pore size distributions of the ABBSC-900. ABBSC-900 is classified as having a type-II isotherm by IUPAC, indicating many micropores in addition to mesopores (Figure S2, insert). The micropores are thought to be involved in charge storage, while the mesopores are thought to be involved in the diffusion of charge carriers. The specific surface area of ABBSC-900 was 79 m^2 g^{-1}, measured on the standard BET method. The average pore diameter is 1.8 nm, and the pore volume is 0.99 cm^3 g^{-1}. Combining the results of the XRD, Raman, and BET investigations, the derived carbon of ABBSC-900 has a moderate surface area and a large interlayer spacing, which are favorable for lithium-ion reversible storage.

3.2. Electrochemical Characterization. In a subsequent stage, a half-cell configuration was used to examine the electrochemical performance of the manufactured samples versus that of Li metal. The cyclic voltammograms (CV) of ABBSC anodes, including ABBSC-700, ABBSC-800, and ABBSC-900, are displayed in Figure 5a–c. These CVs were recorded in the 0.01–3.0 V voltage range vs Li^+/Li with a scan rate of 0.05 mV s^{-1}. The creation of stable solid electrolyte interphase (SEI) on the electrode surface and the electrolyte's breakdown could be the causes of the irreversible cathodic peak that occurs at 0.78 V in the first cycle. Additionally, successive cycles yield identical cyclic voltammograms after the initial cycle, guaranteeing the electrode's cycling stability and stable SEI development. Following this peak, the peak present at ∼0.20 V vs Li^+/Li, respectively, suggests that lithium ions intercalation and deintercalation into the layers of the ABBSC anode are involved in the observed CV behavior. Similar to previously published literature, this peak finding results from the intercalation or deintercalation of lithium ions in their proper places (particularly following progressive cycling, except for the first initial creation cycle).[29,50] Figure 5d shows the first CV cycles of the ABBSC-700, ABBSC-800, and ABBSC-900 anodes. ABBSC-900 anode shows a high current response compared to the ABBSC-700 and ABBSC-800 anodes.

The charge–discharge curves and cycling performance of ABBSC anodes were measured in the voltage range of 0.01–3.0 V at a current density of 500 mA g^{-1}, shown in Figure 6. Figure 6a–c displays the long cycling stability of the ABBSC-700, ABBSC-800, and ABBSC-900 anodes at 500 mA g^{-1}. The initial-discharge specific capacity is 372.5, 388.7, and 593.7 mA h g^{-1} for ABBSC-700, ABBSC-800, and ABBSC-900 anodes, respectively, the high initial-discharge capacities of the anodes due to the formation of SEI during the initial cycle.[51] The charging capacities of ABBSC-700, ABBSC-800, and ABBSC-900 anodes 310.2, 353.2, and 473.7 mA h g^{-1}, and the corresponding Coulombic efficiency is poorer, at 83.2 and 90.8, 80.8%, respectively. Following the formation cycle, the reported discharge capacities for the ABBSC-700, ABBSC-800, and ABBSC-900 anodes steadily decline to 222.5, 311.4, and 483.9 mA h g^{-1} at the 100th cycle, corresponding to an irreversible capacity loss of 60.0, 80.1, and 81.5% respectively, due to the SEI formation in the initial cycle. It is interesting to note that, even at high rates of 500 mA g^{-1}, the ABBSC-900 anode's capacity value is discovered to be superior to that of commercial graphite anodes upon extended cycles and previous publications (Table 3).[33,37,49,52−67] Compared with the ABBSC-700 and ABBSC-800 anodes, the ABBSC-900 anode exhibits a superior electrochemical performance. Figure 6d–f represents the 1st, 50th, 100th, 150th, and 200th charge–discharge curves of ABBSC-700, ABBSC-800, and ABBSC-900 anodes under a current density of 500 mA g^{-1}. After the initial cycle, the ABBSC-700, ABBSC-800, and

https://doi.org/10.1021/acsomega.4c00797
ACS Omega 2024, 9, 16725−16733

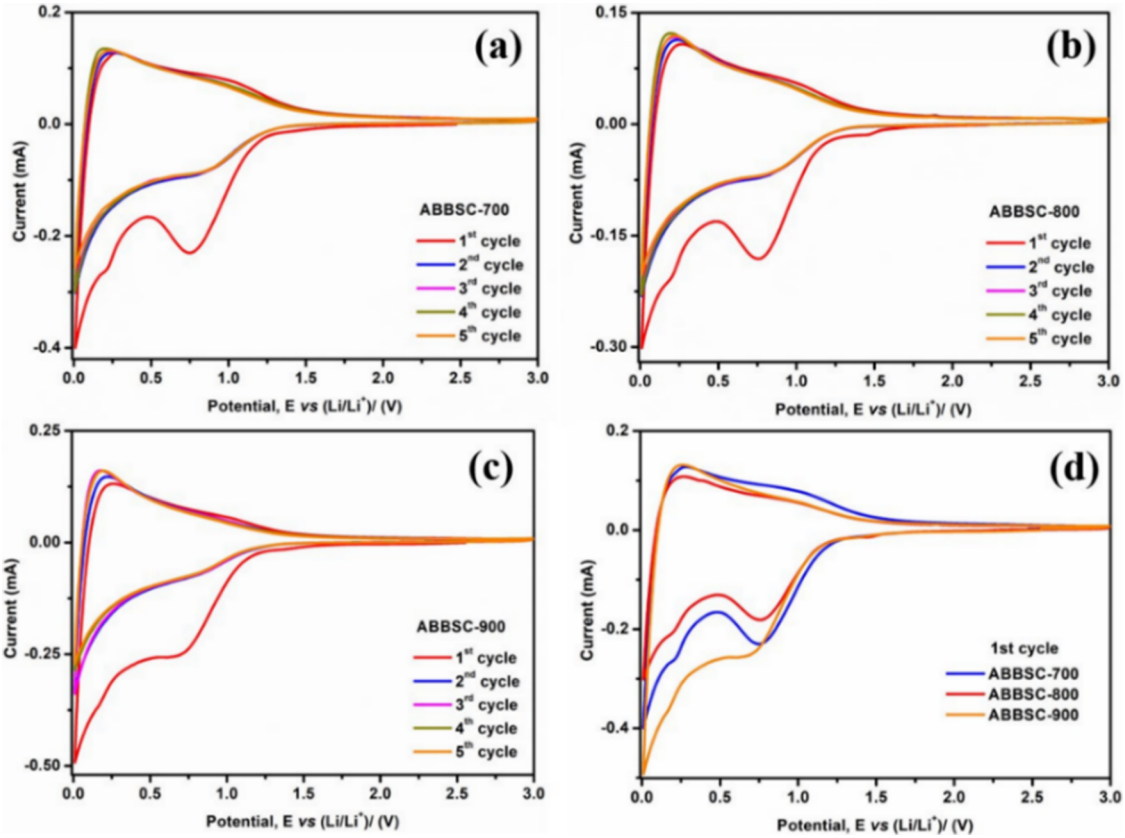

Figure 5. (a−c) Cyclic voltammogram of ABBSC-700, ABBSC-800, and ABBSC-900 anode with scan rate of 0.05 mV s^{-1} and (d) 1st CV cycle curves of the ABBSC-700, ABBSC-800, and ABBSC-900 anodes.

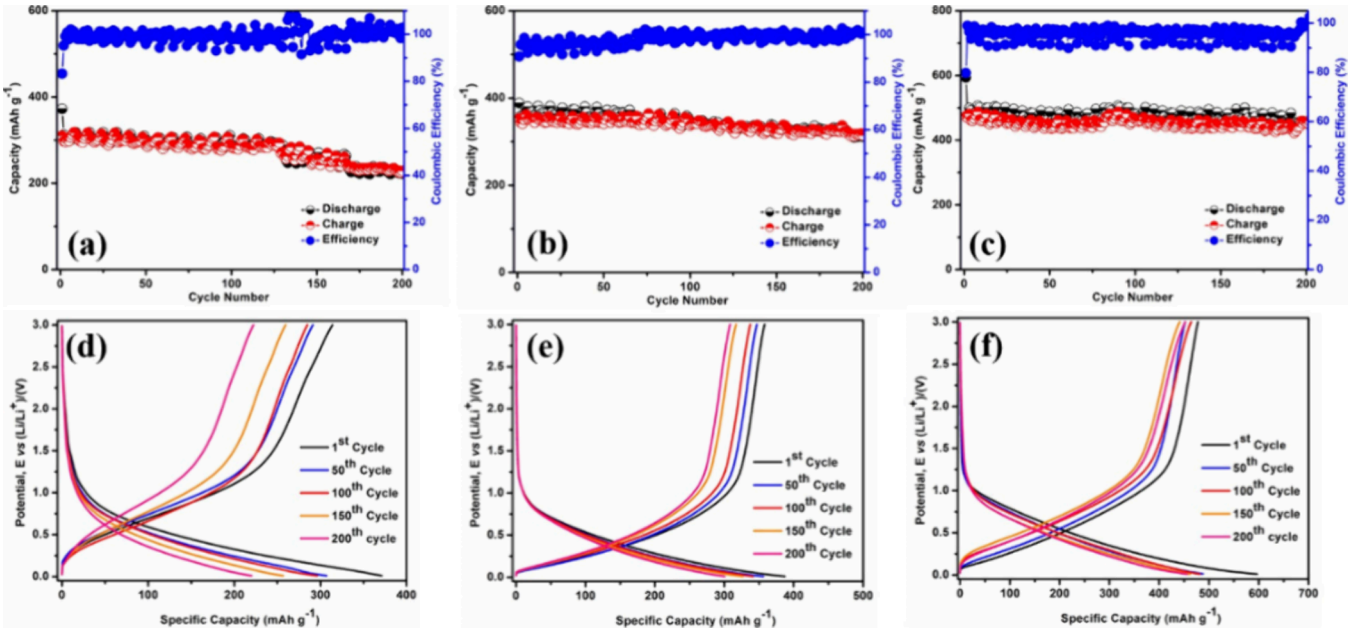

Figure 6. (a−c) Charge−discharge behavior of ABBSC-700, ABBSC-800, and ABBSC-900 anodes at 500 mA g^{-1} current density, (d−f) capacity vs voltage behavior of ABBSC-700, ABBSC-800, and ABBSC-900 anodes 1st, 50th, 100th, 150th, and 200th cycle.

ABBSC-900 anodes showed good reversibility. ABBSC-900 anode outperforms ABBSC-700 and ABBSC-800 in terms of reversible capacity as the temperature rises to 900 °C because of its improved graphitization and regulated surface area, as seen by the Raman spectra and N_2 adsorption/desorption test.

Figure 7 shows the ABBSC-700, ABBSC-800, and ABBSC-900 anodes' best rate capability performance at the current densities of 50, 100, 200, 800, 500, and 1000 mA g^{-1}. Figure S3 displays the charge−discharge profiles of the ABBSC-700, ABBSC-800, and ABBSC-900 anodes under the influence of various current densities. The capacities of ABBSC anodes

https://doi.org/10.1021/acsomega.4c00797
ACS Omega 2024, 9, 16725−16733

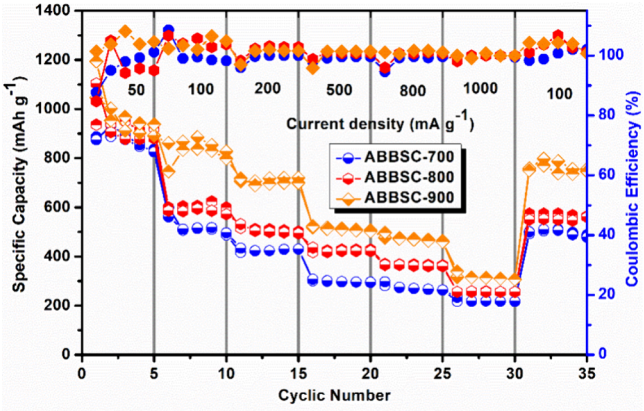

Figure 7. Rate capability behavior of ABBSC-700, ABBSC-800, and ABBSC-900 anodes at various current densities (50, 100, 200, 500, 800, and 1000 mA g^{-1}).

under different current densities are displayed in Table 1. ABBSC-900 anodes deliver reversible capacities of 1046, 862, 706, 518, 476, and 316 mA h g^{-1}, with current densities of 50, 100, 200, 800, 500, and 1000 mA g^{-1}. Subsequently, the capacity recovered to 402.6 mA h g^{-1} when the current density decreased to 100 mA g^{-1}, indicating a high reversibility for ABBSC-900. The reversible capacities at 500 and 1000 mA g^{-1} current densities of the ABBSC-900 anode exhibit better compared to ABBSC-700 and ABBSC-800 anodes. Consequently, ABBSC-900 meets the requirements for high-capacity, low-cost, high-rate anode material for LIBs, creating new opportunities for the development of environmentally benign and commercially viable LIB electrode materials.

Table 1. At Different Current Density Conditions (50−1000 mA g^{-1}) the Capacity Values of ABBSC Anodes (in mA h g^{-1})

	ABBSC-700		ABBSC-800		ABBSC-900	
current density (mA g^{-1})	Q_c	Q_{dc}	Q_c	Q_{dc}	Q_c	Q_{dc}
50	887	875	936	1104	1046	1194
100	598	561	600	586	746	862
200	416	433	516	532	706	718
500	301	307	418	436	518	524
800	281	297	370	366	476	496
1000	217	233	256	256	316	340

The EIS testing aimed to determine the carbons produced from blackberry seeds and their reaction kinetics. EIS measurements were performed at an amplitude of 10 mV and a frequency of 10 kHz to 100 mHz, both before and after cycles at a current density of 500 mA g^{-1}. The Nyquist plots are displayed in Figure 8, with a diagonal straight line in the low frequency and a semicircle (before cycling) in the high and middle frequencies. The diameter of the semicircle is generally proportional to the impedance, which includes the electrolyte resistance (R_s) and charge-transfer resistance (R_{ct}), and it is associated with the charge-transfer process that takes place at the electrode/electrolyte interface. The slope of the straight line is inversely proportional to the Warburg impedance, and the inclination line in the low-frequency region corresponds to the lithium-ion diffusion process inside the electrode. As shown in Figure 8, the ABBCS-900 electrode's semicircle diameter is lower than that of the ABBSC-700 and ABBSC-800 electrodes. In other words, ABBSC-700, ABBSC-800, and ABBSC-900 have recorded initial charge-transfer resistance values of 141, 106, and 68, respectively.

Furthermore, compared to ABBSC-700 and ABBSC-800, the ABBSC-900 anode has a greater slope at low frequencies, indicating the electrode's superior ability to diffuse lithium ions. Additionally, the cells were cycled for 200 cycles at a current density of 500 mA g^{-1}. The collected Nyquist plots provide additional insight into the diffusion of lithium ions involved in the ABBSC anode, particularly during extended cycles. The measured R_{ct} values for the ABBSC-700, ABBSC-800, and ABBSC-900 anodes are 140, 51, and 67, respectively (Table 2), and, still, the ABBSC-900 anodes show a high slope

Table 2. Electrolyte (R_s) and Charge-Transfer Resistance (R_{ct}) of ABBSC Anodes as Fabricated Coin Cells and after 100 Cycles

	before cycling		after cycling	
electrode name	R_s (ohm)	R_{ct} (ohm)	R_s (ohm)	R_{ct} (ohm)
ABBSC-700	6.2	141.5	12.5	140
ABBSC-800	5.2	106.6	14.5	51
ABBSC-900	5.3	68	7.2	67

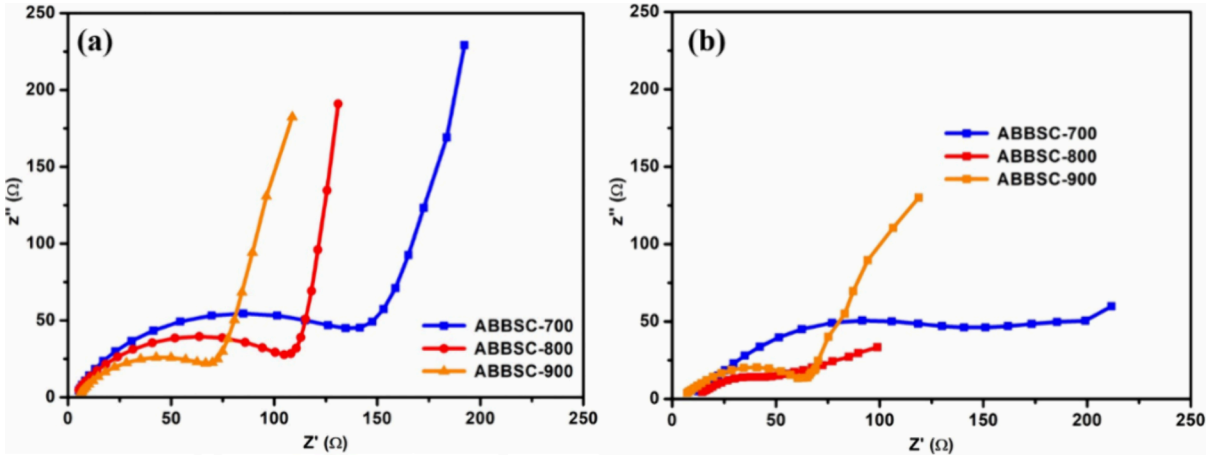

Figure 8. Electrochemical impedance spectroscopy study of as fabricated (a) and after long cycles (b) of ABBSC-700, ABBSC-800, and ABBSC-900 anodes.

https://doi.org/10.1021/acsomega.4c00797
ACS Omega 2024, 9, 16725−16733

at low frequencies. It is concluded that at the electrode/electrolyte interface and within the electrode the ABBSC-900 anode exhibits lower impedances (including R_s and R_{ct}). This shows that compared to ABBSC-700 and ABBSC-800, the ABBSC-900 anode has higher charge transfer and lithium-ion diffusion rate, ultimately leading to improved capacity retention and rate performance (Table 3).

Table 3. Comparison of the Bio-Wastes-Derived Carbon Materials Performance for LIB Anodes

anode materials	synthesis method	current density (mA g^{-1})	reversible capacity (mA h g^{-1})	ref
rice straws	KOH/800 °C/2 h	372	400	33
loofah	KOH/1000 °C/2 h	500	175	37
banana peel	KOH/HCl/1100 °C/5 h	500	600	49
cherry pit	KOH or H_3PO_4/800 °C/2 h	372	150	52
sisal fiber	hydrothermal method	100	247	53
bagasse	KOH/650 °C/1 h	500	280	54
portobello-mushroom	KOH/1100 °C/2 h	100	260	55
mustard seed husks	KOH/800 °C/2 h	500	280	56
tamarind plant Seeds	KOH/500 °C/1 h	200	370	57
jute fiber	$ZnCl_2$/500 °C/1 h	372	420	58
coffee waste grounds	800 °C/2 h	400	212	59
spruce wood	1100 °C/6 h	372	158	60
peanut shell	KOH/600 °C/5 h	372	474	61
coconut oil	H_2SO_4/H_2O_2	400	400	62
soybean	KOH/700 °C/2 h	372	450	63
carrageen	KOH/700 °C/1 h	500	450	64
coconut shells	H_3BO_3/urea/1100 °C/4 h	500	600	65
sweet potato	800 °C/2 h	500	300	66
corn stalk	$CaCl_2$/600 °C/1 h	700	465	67
ABBSC	KOH/900 °C/2 h	500	484 (200th cycle)	this work

4. CONCLUSIONS

Here, we present the effective synthesis of a carbon compound using blackberry seeds, an inexpensive and sustainable source material. Carbon produced from blackberry seeds (ABBSC-700, ABBSC-800, and ABBSC-900) has shown promise as an electrode material for LIBs. As-derived carbon had considerable *d*-spacing, a single-layer graphene sheet that was haphazardly oriented, and a few-layer graphene sheets with a low degree of graphitization after being activated with KOH. In particular, the ABBSC-900 carbon material maintains a moderated surface area (up to 79 m^2 g^{-1}) and micro- and mesoporous character. Among all three anodes, ABBSC-900 shows promise as a superior anode material in reversible specific capacities with excellent rate capability and long-term performance (483.9 mA h g^{-1} with a current density of 500 mA g^{-1}). The anode ABBSC-900 is classified as a filth-to-wealth conversion attempt. It finds extensive use in electrochemical energy storage systems, ensuring its continued significance in materials science. It is only utilized for energy management and a cleaner environment.

ASSOCIATED CONTENT

Supporting Information

The Supporting Information is available free of charge at https://pubs.acs.org/doi/10.1021/acsomega.4c00797.

TEM images of ABBSC-900, nitrogen-sorption isotherms of ABBSC-900 and pore size distributions of the samples obtained from adsorption using the Barrett–Joyner–Halenda (BJH) method (insert), capacity vs voltage profile for (a) ABBSC-700, (b) ABBSC-800, (c) ABBSC-900 anodes at different current density and (d) first cycle charge/discharge profile of three anodes with current density of 50 mA g^{-1} (PDF)

AUTHOR INFORMATION

Corresponding Author

Edreese H. Alsharaeh − *College of Science and General Studies, AlFaisal University, Riyadh 11533, Saudi Arabia;* orcid.org/0000-0002-3707-7883; Email: ealsharaeh@alfaisal.edu

Authors

Chandra Sekhar Bongu − *College of Science and General Studies, AlFaisal University, Riyadh 11533, Saudi Arabia*

Abeer Shiraz Khan − *College of Science and General Studies, AlFaisal University, Riyadh 11533, Saudi Arabia*

Muhammad Arsalan − *EXPEC Advanced Research Center, Saudi Aramco, Dhahran 31311, Saudi Arabia;* orcid.org/0000-0002-1502-8247

Complete contact information is available at: https://pubs.acs.org/10.1021/acsomega.4c00797

Notes

The authors declare no competing financial interest.

ACKNOWLEDGMENTS

This work is part of a research project PIF 726175. The authors gratefully acknowledge Alfaisal University and its Office of Research & Innovation for their continuous support throughout this study.

REFERENCES

(1) Wang, S.; Yata, S.; Nagano, J.; Okano, Y.; Kinoshita, H.; Kikuta, H.; Yamabe, T. A New Carbonaceous Material with Large Capacity and High Efficiency for Rechargeable Li-Ion Batteries. *J. Electrochem. Soc.* **2000**, *147* (7), 2498.

(2) Wu, Y.-P.; Rahm, E.; Holze, R. Carbon Anode Materials for Lithium Ion Batteries. *J. Power Sources* **2003**, *114* (2), 228−236.

(3) Reddy, M. V.; Subba Rao, G.; Chowdari, B. Metal Oxides and Oxysalts as Anode Materials for Li Ion Batteries. *Chem. Rev.* **2013**, *113* (7), 5364−5457.

(4) Oktaviano, H. S.; Yamada, K.; Waki, K. Nano-Drilled Multiwalled Carbon Nanotubes: Characterizations and Application for LIB Anode Materials. *J. Mater. Chem.* **2012**, *22* (48), 25167−25173.

(5) Li, C.; Yin, X.; Chen, L.; Li, Q.; Wang, T. Porous Carbon Nanofibers Derived from Conducting Polymer: Synthesis and

Application in Lithium-Ion Batteries with High-Rate Capability. *J. Phys. Chem. C* **2009**, *113* (30), 13438−13442.
(6) Yoo, E.; Kim, J.; Hosono, E.; Zhou, H.; Kudo, T.; Honma, I. Large Reversible Li Storage of Graphene Nanosheet Families for Use in Rechargeable Lithium Ion Batteries. *Nano Lett.* **2008**, *8* (8), 2277−2282.
(7) Wang, C.; Li, D.; Too, C. O.; Wallace, G. G. Electrochemical Properties of Graphene Paper Electrodes Used in Lithium Batteries. *Chemistry of materials* **2009**, *21* (13), 2604−2606.
(8) Chang, J.; Huang, X.; Zhou, G.; Cui, S.; Hallac, P. B.; Jiang, J.; Hurley, P. T.; Chen, J. Multilayered Si Nanoparticle/Reduced Graphene Oxide Hybrid as a High-Performance Lithium-Ion Battery Anode. *Advanced Materials (Deerfield Beach, Fla.)* **2014**, *26* (5), 758−764.
(9) Chen, J.; Wang, J.; Zhang, S.; Xue, K.; Zhang, J.; Cao, F.; Kong, Q.; Guo, X. Si Nanoparticles Confined in N, P-Doped Double Carbon as Efficient Anode Materials for Lithium Ion Batteries. *J. Alloys Compd.* **2023**, *935*, No. 167850.
(10) Ji, H.; Chen, Q.; Hua, K.; Ma, Q.; Wang, R.; Zhang, L.; Zhang, C. Si Nanoparticles Embedded in Porous N-Doped Carbon Fibers as a Binder-Free and Flexible Anode for High-Performance Lithium-Ion Batteries. *J. Alloys Compd.* **2023**, *936*, No. 168256.
(11) Zhu, Z.; Wang, S.; Du, J.; Jin, Q.; Zhang, T.; Cheng, F.; Chen, J. Ultrasmall Sn Nanoparticles Embedded in Nitrogen-Doped Porous Carbon as High-Performance Anode for Lithium-Ion Batteries. *Nano Lett.* **2014**, *14* (1), 153−157.
(12) Li, W.-L.; Lai, H.; Sun, C.-H.; Lin, Y.-Y.; Sun, Y.-H.; Nan, J.-M. Heterojunction of SnO2/Sn Nanoparticles Coated by Graphene-like Porous Carbon as Ultrahigh Capacity Anode of Lithium-Ion Batteries. *J. Alloys Compd.* **2023**, *948*, No. 169811.
(13) Li, Y.; Ren, H.; Zhao, Y.; Guo, Z.; Ma, C.; Wu, R.; Chen, C.; Zhao, Y. A Facile Complexing Chemical Reduction for the Preparation of Sn/Graphene Nanocomposites and Their High Performance for Lithium-Ion Batteries. *J. Alloys Compd.* **2023**, *937*, No. 168421.
(14) Grugeon, S.; Laruelle, S.; Herrera-Urbina, R.; Dupont, L.; Poizot, P.; Tarascon, J. Particle Size Effects on the Electrochemical Performance of Copper Oxides toward Lithium. *J. Electrochem. Soc.* **2001**, *148* (4), A285.
(15) Liang, B.; Yang, T.; Yang, H.; Zhao, J.; Dong, Y. Preparation of CuO@ Humic Acid@ Carbon Nanotube Composite Material Using Humic Acid as a Coupling Agent and Its Lithium-Ion Storage Performance. *RSC Adv.* **2023**, *13* (35), 24191−24200.
(16) Zhang, Z.; Ran, K.; Wang, W.; Cao, S.; Zhao, R.; Zhou, H.; Xue, W.; Li, H.; Wang, W.; Min, Z.; Jiang, K.; Wang, K. Plasma-Induced Oxygen Defects in Titanium Dioxide to Address the Long-Term Stability of Pseudocapacitive MnO2 Anode for Lithium Ion Batteries. *J. Colloid Interface Sci.* **2024**, *656*, 116−124, DOI: 10.1016/j.jcis.2023.11.087.
(17) Lin, Y.; Tian, H.; Qian, J.; Yu, M.; Hu, T.; Lassi, U.; Chen, Z.; Wu, Z. Biocarbon-Directed Vertical δ-MnO2 Nanoflakes for Boosting Lithium-Ion Diffusion Kinetics. *Materials Today Chemistry* **2022**, *26*, No. 101023.
(18) Sekhar, B. C.; Babu, G.; Kalaiselvi, N. Nanoflake Driven Mn 2 O 3 Microcubes Modified with Cooked Rice Derived Carbon for Improved Electrochemical Behavior. *RSC Adv.* **2015**, *5* (6), 4568−4577.
(19) Zhang, L.; Wu, H. B.; Madhavi, S.; Hng, H. H.; Lou, X. W. Formation of Fe2O3Microboxes with Hierarchical Shell Structures from Metal−Organic Frameworks and Their Lithium Storage Properties. *J. Am. Chem. Soc.* **2012**, *134* (42), 17388−17391.
(20) Li, Z.; Mao, Y.; Tian, Q.; Zhang, W.; Yang, L. Extremely Facile Preparation of High-Performance Fe2O3 Anode for Lithium-Ion Batteries. *J. Alloys Compd.* **2019**, *784*, 125−133.
(21) Pan, Y.; Luo, C.; Yang, D.; Sun, P.; Chen, J.; Sui, Z.; Tian, Q. Coordination Chemistry-Assisted Ecofriendly Preparation of Fe2O3 Nanoparticles Embedded in Hierarchical Carbon for Improved Lithium Storage. *J. Alloys Compd.* **2023**, *962*, No. 171153.
(22) Zhang, H.; Wang, F.; Wang, Y.; Wei, H.; Zhang, W.; Cao, R.; Zheng, H. Two-Dimensional Hollow Carbon Skeleton Decorated with Ultrafine Co3O4 Nanoparticles for Enhanced Lithium Storage. *J. Colloid Interface Sci.* **2023**, *631*, 191−200.
(23) Wakihara, M. Recent Developments in Lithium Ion Batteries. *Materials Science and Engineering: R: Reports* **2001**, *33* (4), 109−134.
(24) Noel, M.; Suryanarayanan, V. Role of Carbon Host Lattices in Li-Ion Intercalation/de-Intercalation Processes. *J. Power Sources* **2002**, *111* (2), 193−209.
(25) Wang, Z.; Zhou, L.; Lou, X. W. Metal Oxide Hollow Nanostructures for Lithium-ion Batteries. *Adv. Mater.* **2012**, *24*, 1903−1911, DOI: 10.1002/adma.201200469.
(26) Chen, Y.; Guo, X.; Liu, A.; Zhu, H.; Ma, T. Recent Progress in Biomass-Derived Carbon Materials Used for Secondary Batteries. *Sustainable Energy & Fuels* **2021**, *5* (12), 3017−3038.
(27) Ruiz, V.; Blanco, C.; Granda, M.; Santamaría, R. Enhanced Life-Cycle Supercapacitors by Thermal Treatment of Mesophase-Derived Activated Carbons. *Electrochim. Acta* **2008**, *54* (2), 305−310.
(28) Roldan, S.; Villar, I.; Ruíz, V.; Blanco, C.; Granda, M.; Menendez, R.; Santamaria, R. Comparison between Electrochemical Capacitors Based on NaOH-and KOH-Activated Carbons. *Energy Fuels* **2010**, *24* (6), 3422−3428.
(29) Saravanan, K.; Kalaiselvi, N. Nitrogen Containing Bio-Carbon as a Potential Anode for Lithium Batteries. *Carbon* **2015**, *81*, 43−53.
(30) Arrebola, J.; Caballero, A.; Hernán, L.; Morales, J.; Olivares-Marín, M.; Gómez-Serrano, V. Improving the Performance of Biomass-Derived Carbons in Li-Ion Batteries by Controlling the Lithium Insertion Process. *J. Electrochem. Soc.* **2010**, *157* (7), A791.
(31) Han, S.-W.; Jung, D.-W.; Jeong, J.-H.; Oh, E.-S. Effect of Pyrolysis Temperature on Carbon Obtained from Green Tea Biomass for Superior Lithium Ion Battery Anodes. *Chemical Engineering Journal* **2014**, *254*, 597−604.
(32) Wang, L.; Xue, J.; Gao, B.; Gao, P.; Mou, C.; Li, J. Rice Husk Derived Carbon−Silica Composites as Anodes for Lithium Ion Batteries. *RSC Adv.* **2014**, *4* (110), 64744−64746.
(33) Zhang, F.; Wang, K.-X.; Li, G.-D.; Chen, J.-S. Hierarchical Porous Carbon Derived from Rice Straw for Lithium Ion Batteries with High-Rate Performance. *Electrochem. Commun.* **2009**, *11* (1), 130−133.
(34) Rufford, T. E.; Hulicova-Jurcakova, D.; Khosla, K.; Zhu, Z.; Lu, G. Q. Microstructure and Electrochemical Double-Layer Capacitance of Carbon Electrodes Prepared by Zinc Chloride Activation of Sugar Cane Bagasse. *J. Power Sources* **2010**, *195* (3), 912−918.
(35) Rufford, T. E.; Hulicova-Jurcakova, D.; Zhu, Z.; Lu, G. Q. Nanoporous Carbon Electrode from Waste Coffee Beans for High Performance Supercapacitors. *Electrochem. Commun.* **2008**, *10* (10), 1594−1597.
(36) Hwang, Y. J.; Jeong, S.; Shin, J.; Nahm, K. S.; Stephan, A. M. High Capacity Disordered Carbons Obtained from Coconut Shells as Anode Materials for Lithium Batteries. *J. Alloys Compd.* **2008**, *448* (1−2), 141−147.
(37) Wu, Z.; Wang, L.; Huang, J.; Zou, J.; Chen, S.; Cheng, H.; Jiang, C.; Gao, P.; Niu, X. Loofah-Derived Carbon as an Anode Material for Potassium Ion and Lithium Ion Batteries. *Electrochim. Acta* **2019**, *306*, 446−453.
(38) Zhang, Y.; Chen, L.; Meng, Y.; Xie, J.; Guo, Y.; Xiao, D. Lithium and Sodium Storage in Highly Ordered Mesoporous Nitrogen-Doped Carbons Derived from Honey. *J. Power Sources* **2016**, *335*, 20−30.
(39) Tao, L.; Huang, Y.; Yang, X.; Zheng, Y.; Liu, C.; Di, M.; Zheng, Z. Flexible Anode Materials for Lithium-Ion Batteries Derived from Waste Biomass-Based Carbon Nanofibers: I. Effect of Carbonization Temperature. *RSC Adv.* **2018**, *8* (13), 7102−7109.
(40) Zhang, X.; Hu, J.; Chen, X.; Zhang, M.; Huang, Q.; Du, X.; Liu, Y.; Li, X. Microtubular Carbon Fibers Derived from Bamboo and Wood as Sustainable Anodes for Lithium and Sodium Ion Batteries. *Journal of Porous Materials* **2019**, *26*, 1821−1830.
(41) Choe, U.; Li, Y.; Yu, L.; Gao, B.; Wang, T. T.; Sun, J.; Chen, P.; Yu, L. Chemical Composition of Cold-pressed Blackberry Seed Flour

https://doi.org/10.1021/acsomega.4c00797
ACS Omega 2024, 9, 16725−16733

Extract and Its Potential Health-beneficial Properties. *Food science & nutrition* **2020**, *8* (2), 1215−1225.
(42) Wang, J.; Lian, P.; Yu, Q.; Wei, J.; Kang, W. Antithrombotic Mechanism of Polysaccharides in Blackberry (Rubus Spp.) Seeds. *Food Nutr. Res.* **2017**, *61*, No. 1379862, DOI: 10.1080/16546628.2017.1379862.
(43) Verma, R.; Gangrade, T.; Punasiya, R.; Ghulaxe, C. Rubus Fruticosus (Blackberry) Use as an Herbal Medicine. *Pharmacognosy reviews* **2014**, *8* (16), 101.
(44) Hameed, A.; Galli, M.; Adamska-Patruno, E.; Krętowski, A.; Ciborowski, M. Select Polyphenol-Rich Berry Consumption to Defer or Deter Diabetes and Diabetes-Related Complications. *Nutrients* **2020**, *12* (9), 2538.
(45) Kubota, K.; Shimadzu, S.; Yabuuchi, N.; Tominaka, S.; Shiraishi, S.; Abreu-Sepulveda, M.; Manivannan, A.; Gotoh, K.; Fukunishi, M.; Dahbi, M.; Komaba, S. Structural Analysis of Sucrose-Derived Hard Carbon and Correlation with the Electrochemical Properties for Lithium, Sodium, and Potassium Insertion. *Chem. Mater.* **2020**, *32* (7), 2961−2977.
(46) Wu, F.; Zhang, M.; Bai, Y.; Wang, X.; Dong, R.; Wu, C. Lotus Seedpod-Derived Hard Carbon with Hierarchical Porous Structure as Stable Anode for Sodium-Ion Batteries. *ACS Appl. Mater. Interfaces* **2019**, *11* (13), 12554−12561.
(47) Liu, Y.; Xue, J.; Zheng, T.; Dahn, J. Mechanism of Lithium Insertion in Hard Carbons Prepared by Pyrolysis of Epoxy Resins. *Carbon* **1996**, *34* (2), 193−200.
(48) Sadezky, A.; Muckenhuber, H.; Grothe, H.; Niessner, R.; Pöschl, U. Raman Microspectroscopy of Soot and Related Carbonaceous Materials: Spectral Analysis and Structural Information. *Carbon* **2005**, *43* (8), 1731−1742.
(49) Lotfabad, E. M.; Ding, J.; Cui, K.; Kohandehghan, A.; Kalisvaart, W. P.; Hazelton, M.; Mitlin, D. High-Density Sodium and Lithium Ion Battery Anodes from Banana Peels. *ACS Nano* **2014**, *8* (7), 7115−7129.
(50) Jain, A.; Aravindan, V.; Jayaraman, S.; Kumar, P. S.; Balasubramanian, R.; Ramakrishna, S.; Madhavi, S.; Srinivasan, M. Activated Carbons Derived from Coconut Shells as High Energy Density Cathode Material for Li-Ion Capacitors. *Sci. Rep.* **2013**, *3* (1), 3002.
(51) Su, D. S.; Schlögl, R. Nanostructured Carbon and Carbon Nanocomposites for Electrochemical Energy Storage Applications. *ChemSusChem* **2010**, *3* (2), 136−168, DOI: 10.1002/cssc.200900182.
(52) Hernández-Rentero, C.; Marangon, V.; Olivares-Marín, M.; Gómez-Serrano, V.; Caballero, Á.; Morales, J.; Hassoun, J. Alternative Lithium-Ion Battery Using Biomass-Derived Carbons as Environmentally Sustainable Anode. *J. Colloid Interface Sci.* **2020**, *573*, 396−408.
(53) Yu, X.; Zhang, K.; Tian, N.; Qin, A.; Liao, L.; Du, R.; Wei, C. Biomass Carbon Derived from Sisal Fiber as Anode Material for Lithium-Ion Batteries. *Mater. Lett.* **2015**, *142*, 193−196.
(54) Zheng, S.; Luo, Y.; Zhang, K.; Liu, H.; Hu, G.; Qin, A. Nitrogen and Phosphorus Co-Doped Mesoporous Carbon Nanosheets Derived from Bagasse for Lithium-Ion Batteries. *Mater. Lett.* **2021**, *290*, No. 129459.
(55) Campbell, B.; Ionescu, R.; Favors, Z.; Ozkan, C. S.; Ozkan, M. Bio-Derived, Binderless, Hierarchically Porous Carbon Anodes for Li-Ion Batteries. *Sci. Rep.* **2015**, *5* (1), No. 14575.
(56) Pramanik, A.; Chattopadhyay, S.; De, G.; Mahanty, S. Efficient Energy Storage in Mustard Husk Derived Porous Spherical Carbon Nanostructures. *Materials Advances* **2021**, *2* (22), 7463−7472.
(57) Panda, M. R.; Kathribail, A. R.; Modak, B.; Sau, S.; Dutta, D. P.; Mitra, S. Electrochemical Properties of Biomass-Derived Carbon and Its Composite along with Na2Ti3O7 as Potential High-Performance Anodes for Na-Ion and Li-Ion Batteries. *Electrochim. Acta* **2021**, *392*, No. 139026.
(58) Dou, Y.; Liu, X.; Wang, X.; Yu, K.; Liang, C. Jute Fiber Based Micro-Mesoporous Carbon: A Biomass Derived Anode Material with High-Performance for Lithium-Ion Batteries. *Materials Science and Engineering: B* **2021**, *265*, No. 115015.
(59) Luna-Lama, F.; Rodríguez-Padrón, D.; Puente-Santiago, A. R.; Muñoz-Batista, M. J.; Caballero, A.; Balu, A. M.; Romero, A. A.; Luque, R. Non-Porous Carbonaceous Materials Derived from Coffee Waste Grounds as Highly Sustainable Anodes for Lithium-Ion Batteries. *Journal of Cleaner Production* **2019**, *207*, 411−417.
(60) Drews, M.; Büttner, J.; Bauer, M.; Ahmed, J.; Sahu, R.; Scheu, C.; Vierrath, S.; Fischer, A.; Biro, D. Spruce Hard Carbon Anodes for Lithium-Ion Batteries. *ChemElectroChem.* **2021**, *8* (24), 4750−4761.
(61) Lv, W.; Wen, F.; Xiang, J.; Zhao, J.; Li, L.; Wang, L.; Liu, Z.; Tian, Y. Peanut Shell Derived Hard Carbon as Ultralong Cycling Anodes for Lithium and Sodium Batteries. *Electrochim. Acta* **2015**, *176*, 533−541.
(62) Gaddam, R. R.; Yang, D.; Narayan, R.; Raju, K.; Kumar, N. A.; Zhao, X. Biomass Derived Carbon Nanoparticle as Anodes for High Performance Sodium and Lithium Ion Batteries. *Nano energy* **2016**, *26*, 346−352.
(63) Zhang, D.; Wang, G.; Xu, L.; Lian, J.; Bao, J.; Zhao, Y.; Qiu, J.; Li, H. Defect-Rich N-Doped Porous Carbon Derived from Soybean for High Rate Lithium-Ion Batteries. *Appl. Surf. Sci.* **2018**, *451*, 298−305.
(64) Lu, M.; Yu, W.; Shi, J.; Liu, W.; Chen, S.; Wang, X.; Wang, H. Self-Doped Carbon Architectures with Heteroatoms Containing Nitrogen, Oxygen and Sulfur as High-Performance Anodes for Lithium-and Sodium-Ion Batteries. *Electrochim. Acta* **2017**, *251*, 396−406.
(65) Chen, S.; Yang, H.; Chen, Q.; Liu, L.; Hou, X.; Luo, L.; Lin, C.; Li, C.; Chen, Y. Synthesis of BCN Nanoribbons from Coconut Shells Using as High-Performance Anode Materials for Lithium-Ion Batteries. *Electrochim. Acta* **2020**, *346*, No. 136239.
(66) Zheng, P.; Liu, T.; Zhang, J.; Zhang, L.; Liu, Y.; Huang, J.; Guo, S. Sweet Potato-Derived Carbon Nanoparticles as Anode for Lithium Ion Battery. *RSC Adv.* **2015**, *5* (51), 40737−40741.
(67) Li, Y.; Li, C.; Qi, H.; Yu, K.; Li, X. Formation Mechanism and Characterization of Porous Biomass Carbon for Excellent Performance Lithium-Ion Batteries. *RSC Adv.* **2018**, *8* (23), 12666−12671.

https://doi.org/10.1021/acsomega.4c00797
ACS Omega 2024, 9, 16725−16733